

Analysis of silicon nitride partial Euler waveguide bends

FLORIAN VOGELBACHER,^{1,2,*} STEFAN NEVLACSIL,¹
MARTIN SAGMEISTER,³ JOCHEN KRAFT,³ KARL UNTERRAINER,²
AND RAINER HAINBERGER¹

¹AIT Austrian Institute of Technology GmbH, Center for Health & Bioresources, Giefinggasse 4, 1210 Vienna, Austria

²TU Wien, Photonics Institute, Gusshausstraße 27-29, 1040 Vienna, Austria

³ams AG, Tobelbader Straße 30, 8141 Premstätten, Austria

*florian.vogelbacher@tuwien.ac.at

Abstract: In this work we present a detailed analysis of individual loss mechanisms in silicon nitride partial Euler bends at a wavelength of 850 nm. This structure optimizes the transmission through small radii optical waveguide bends. The partial Euler bend geometry balances losses arising from the transition from the straight to the bend waveguide mode, and radiative losses of the bend waveguide mode. Numerical analyses are presented for 45-degree bends commonly employed in S-bend configurations to create lateral offsets, as well as 90- and 180-degree bends. Additionally, 90-degree partial Euler bends were fabricated on a silicon nitride photonic platform to experimentally complement the theoretical findings. The optimized waveguide bends allow for a reduced effective radius without increasing the total bend loss and, thus, enable a higher component density in photonic integrated circuits.

© 2019 Optical Society of America under the terms of the [OSA Open Access Publishing Agreement](#)

1. Introduction

Photonic integrated circuits (PICs) play an important role in data- and telecommunication [1, 2] and are attracting increasing interest in other fields of applications such as astronomy [3, 4], biosensing [5, 6], medical diagnostics [7, 8], and quantum photonics [9]. These applications benefit from the strongly confined light, stable operation, and the small footprint compared to bulk optics. However, the compactness of a PIC is significantly limited by losses arising from waveguide bends used in routing of optical signals. Therefore, the optimization of bends is of pivotal importance in the design of high-density PICs or devices requiring ultra-low losses.

Different approaches to reduce total bend losses have been proposed in literature. For example, a lateral offset between the incoming straight waveguide and the bend can reduce the mode mismatch between these two sections [10]. However, this technique relies on a high fabrication resolution, which is not always attainable by standard photolithography methods. Fabrication limitations are relaxed when a smooth transition between the straight waveguide and the bend is introduced. Ideally, such a transition allows to adiabatically convert the mode profile of a straight waveguide to that of a bent section. In the matched bend approach the length of the bend is optimized to minimize the higher order leaky modes at the output of the bend [11]. Alternatively, a variation of the waveguide width, a multi-step patterning with grooves along the bend or subwavelength gratings on the waveguide can alter the mode confinement and reduce losses in the bend [12–14]. The implementation of grooves and subwavelength gratings requires additional fabrication steps and increases costs. In many applications a bend loss reduction by an optimized geometry alone is therefore favorable. Various bend geometries have been proposed, e.g. based on spline curves [12], trigonometric functions [15], or deduced from a topology optimization [16–19]. The variational method [20, 21] relies on analytic bend loss models for deriving an optimized bend geometry. However, this approach is inherently limited

by the physical validity of the applied bend loss model and, thus, carries the risk of omitting or inadequately describing critical loss mechanisms.

A bend geometry of particular interest is based on the Euler spiral, also known as a clothoid. Euler spirals are widely employed in civil engineering as transition curves because of the continuous change in curvature and straightforward implementation [22, 23]. An Euler spiral is defined through a linear increase of the bend curvature along the path length, resulting in a continuous transition from the straight waveguide to the waveguide bend. This transition reduces the excitation of higher order modes [24]. Optical waveguide bends based on Euler spirals have been successfully demonstrated for single mode and multimode optical waveguides [24, 25]. The combination of an Euler bend with a section of constant curvature has been presented by Fujisawa et al. for a silicon photonic platform in [26]. This combination balances two major loss components of a waveguide bend, namely the transition losses arising from a changing curvature, and radiative losses inherent to a bend waveguide mode.

In this work, we present a detailed numerical analysis of the partial Euler bend geometry. A reformulated description to construct the partial Euler bend geometry compared to the work of Fujisawa et al. [26] facilitates the implementation. This formulation allows to implement arbitrary angled bends $< 360^\circ$. Here, we optimize the partial Euler bend parameter for 45° , 90° and 180° bends for a low-loss silicon nitride photonic platform [8, 27–29] at a wavelength of 850 nm. In difference to previous publications of other groups analyzing various kinds of waveguide bend geometries, our numerical analysis is based on the eigenmode expansion method, which allows a separation of the total losses into bend mode radiation and transition losses along the geometry. This separation provides a valuable insight into the individual contributions to the total loss. Bend angles larger than 180° , which are used for instance in Sagnac loop mirrors [30, 31], can also be constructed with the presented formalism but are not addressed in this work. In addition to the in-depth numerical analysis, we present experimental results on the bend losses of partial Euler bends with an effective radius of $50\ \mu\text{m}$ fabricated on a silicon nitride photonic platform.

2. Theory

In this section, the geometric properties of an Euler spiral are presented and subsequently used for the construction of a partial Euler bend consisting of a section with linearly increasing curvature and a section of constant curvature. Figure 1(a) exemplarily depicts the geometry of a 90° partial Euler bend and indicates the parameters used to describe a partial Euler bend. The bend parameter p relates to the portion of the bend having a linearly increasing curvature. The input and output of a partial Euler bend with effective radius R_{eff} coincide with that of a circular bend of the same radius. The tangent lines of the input and output are preserved. The bend geometry is expressed in Cartesian coordinates to enable a straightforward implementation in a photonic design software.

2.1. The Euler spiral

In Cartesian coordinates the Euler spiral can be constructed through the scaled Fresnel integrals [32]

$$x(s) = \int_0^s \cos\left(\frac{t^2}{2R_0^2}\right) dt \quad (1a)$$

$$y(s) = \int_0^s \sin\left(\frac{t^2}{2R_0^2}\right) dt \quad (1b)$$

where s denotes the path length and R_0 is a free to choose radius. For example, this parameter can be set to $1/\sqrt{2}$ unit length for ease of calculation of the Fresnel integrals. The curvature κ

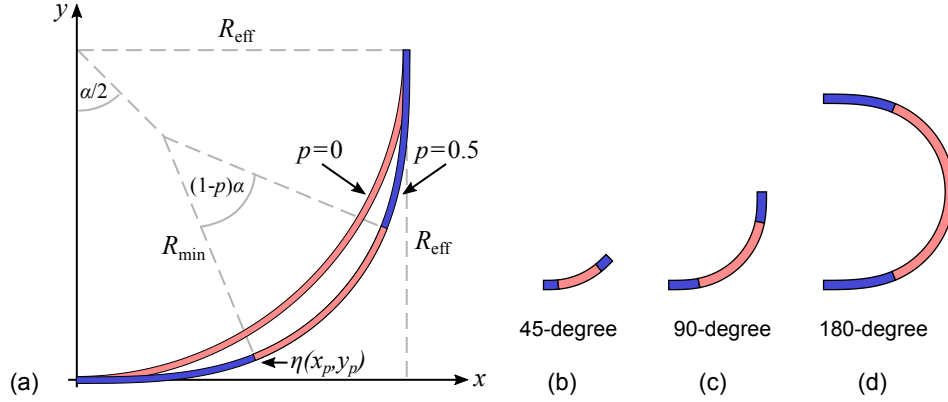


Fig. 1. (a) Geometry of a 90° partial Euler bend with bend parameter $p = 0.5$ and a circular bend. The design parameter p influences the angle at which the transition between the section of linearly increasing curvature (blue) to the section with constant curvature (light red) occurs. For $p = 0$ the partial Euler bend is equivalent to a circular bend. The middle section has a radius of curvature of R_{\min} . (b) 45°, (c) 90°, and (d) 180° bend geometries for $p = 0.2$.

increases linearly with the path length, i.e.,

$$\kappa(s) = \frac{s}{R_0^2} \quad (2)$$

and the angle α is reached at a path length

$$s(\alpha) = R_0 \sqrt{2\alpha}. \quad (3)$$

The curvature at an angle α is accordingly given by

$$\kappa(\alpha) = \frac{\sqrt{2\alpha}}{R_0}. \quad (4)$$

The integrals in Eq. (1a) and Eq. (1b) cannot be solved analytically, but numerical integration or a series expansion can be used to solve these with suitable precision [32–35].

2.2. The partial Euler bend for arbitrary angles

The presented partial Euler bend of total bend angle α is designed symmetrically around $\alpha/2$. In the following the first half of the bend is described. The first section up to an angle $p\alpha/2$ is an Euler spiral, followed by a section with constant radius of curvature up to the angle $\alpha/2$. The second half is readily obtained from a mirroring operation. To construct a partial Euler bend with an effective radius R_{eff} , the functions describing the bend need to be rescaled. The rescaling factor depends on the bend angle α , the effective radius R_{eff} , and the bend parameter p .

In a first step, the coordinates (x_p, y_p) of the end of the Euler section are calculated from Eq. (1a) and Eq. (1b), i.e., $x_p = x(s_p)$ and $y_p = y(s_p)$, where $s_p = R_0 \sqrt{p\alpha}$ denotes the path length to reach the angle $p\alpha/2$. The radius of curvature R_p at (x_p, y_p) is given from Eq. (2), and results in

$$R_p = \frac{1}{\kappa(s_p)} = \frac{R_0}{\sqrt{p\alpha}}. \quad (5)$$

The offset to translate the start of the circular section to the end of the Euler section is calculated with

$$\Delta x = x_p - R_p \sin(p\alpha/2) \quad (6a)$$

$$\Delta y = y_p - R_p [1 - \cos(p\alpha/2)]. \quad (6b)$$

The total bend length is the sum of the path lengths of two Euler sections and the circular section with radius R_p resulting in

$$s_0 = 2s_p + R_p\alpha(1 - p). \quad (7)$$

Combining the results, the functions describing the first half of the unscaled partial Euler bend for angles smaller than $\alpha/2$ are

$$x_{\text{bend}}(s) = \begin{cases} x(s) & \text{for } 0 \leq s \leq s_p \\ R_p \sin\left(\frac{s-s_p}{R_p} + \frac{p\alpha}{2}\right) + \Delta x & \text{for } s_p < s \leq s_0/2 \end{cases} \quad (8a)$$

and

$$y_{\text{bend}}(s) = \begin{cases} y(s) & \text{for } 0 \leq s \leq s_p \\ R_p \left[1 - \cos\left(\frac{s-s_p}{R_p} + \frac{p\alpha}{2}\right)\right] + \Delta y & \text{for } s_p < s \leq s_0/2 \end{cases} \quad (8b)$$

From geometric considerations we find the rescaling factor η to achieve an effective radius R_{eff} to be

$$\eta = \frac{R_{\text{eff}}}{y_{\text{bend}}(s_0/2) + x_{\text{bend}}(s_0/2) / \tan(\alpha/2)}. \quad (9)$$

The equations describing the rescaled bend can be written as

$$\tilde{x}_{\text{bend}}(s) = \eta \cdot x_{\text{bend}}(s/\eta) \quad (10a)$$

$$\tilde{y}_{\text{bend}}(s) = \eta \cdot y_{\text{bend}}(s/\eta). \quad (10b)$$

with the minimum radius of curvature given by

$$R_{\text{min}} = \eta \cdot R_p. \quad (11)$$

The path length to construct the first half of the rescaled bend ranges from

$$0 \leq s \leq \eta \frac{s_0}{2}. \quad (12)$$

The geometric construction allows for bend angles $< 360^\circ$. However, the denominator of the rescale factor η in Eq. (9) depends on the parameter p of the partial Euler bend as well as on the bend angle α . For a bend angle of approximately 263.3° and $p = 1$ the denominator vanishes. In this case, no solution for a pure Euler bend exists but partial Euler bends with a circular section are still possible. For larger bend angles, the maximal possible bend parameter continuously decreases. For example, for a 270° bend the maximum value of the bend parameter is $p = 0.585$. Close to such a singularity in Eq. (9) the arc length and footprint of the partial Euler bend increases significantly. For the studied bends with $\alpha \leq 180^\circ$ no singularity occurs and the minimum radius of curvature R_{min} is always smaller than the effective radius R_{eff} for all $0 < p \leq 1$.

Figure 2 plots the normalized curvature κR_{eff} profiles for four different values of the bend parameter p for a 90° bend, i.e. $p = 0, 0.05, 0.2,$ and 1 . The path length is normalized to the arc length $L_0 = R_{\text{eff}}\pi/2$ of a circular bend. The total path length does not change significantly for

different values of the parameter p . The first derivative of the curvature is not continuous at the transition point between the Euler and the circular section. This singularity does not introduce additional losses because the curvature is continuous and, thus, the mode profile does not change at this transition. The curvature in the middle of a pure Euler bend ($p = 1$) is 82 % higher than that of a circular bend with constant radius. This causes increased radiative bend mode losses compared to a circular bend. On the other hand, for a circular bend the abrupt change in curvature at the interface between the straight and the bent section induces a mode mismatch. A balance between the two extreme geometries optimizes the total loss.

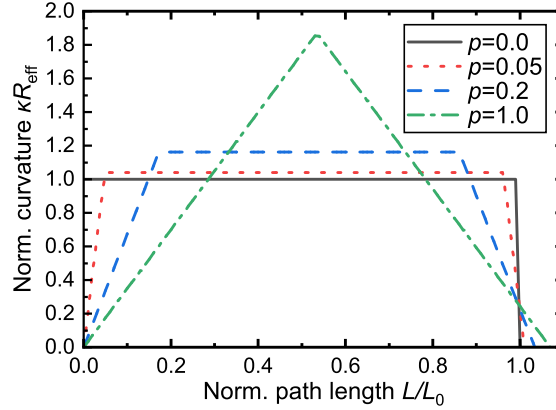


Fig. 2. Normalized curvature along a 90° bend depending on the value of parameter p . The path length L is normalized to the arc length L_0 of a circular bend. A pure Euler bend ($p = 1$) shows an 82 % increased curvature compared to a circular bend ($p = 0$), which increases radiative bend mode losses. The normalized path lengths of partial Euler bends with $p > 0$ are larger than unity.

3. Numerical analysis

3.1. Simulation setup and parameters

The modal power and the bend mode radiation in the partial Euler bend geometries were numerically determined with the commercial eigenmode expansion (EME) method tool FIMMPROP (PhotonD, FIMMWAVE) [36]. The software employs a fully vectorial complex finite difference mode solver that allows the calculations of eigenmodes in a bent waveguide section. The imaginary part of the propagation constant of such an eigenmode reflects its radiative loss. The Euler section with linearly increasing/decreasing curvature was divided into 64 bend subsections of equal path length Δs . A single section was used for the circular bend section. The symmetry of the Euler bend at $\alpha/2$ was exploited to reduce the computation time since only eigenmodes of the first half of the partial Euler bend were calculated. Straight sections at the beginning and end of the partial Euler bend were used to include the losses from the mode mismatch between the straight waveguide input/output and the bend. The transition loss arising from the gradual change of curvature is derived from the difference between total loss and radiative bend mode loss. The EME method is highly suitable for bend radii, at which the computational domain for FDTD would become too large to efficiently be solved.

The investigated wavelength was 850 nm and the refractive indices of silicon nitride and silicon dioxide were assumed to be 2.02 and 1.46, respectively [37, 38]. For this generic silicon nitride photonic platform absorption, scattering, and substrate leakage are neglected because advanced fabrication technologies allow for $< 1 \text{ dB cm}^{-1}$ propagation losses in the visible and near-infrared

wavelength region [8, 27–29]. Therefore, transition and radiative bend mode losses dominate for bends with small radii. The total path length changes only slightly for different values of the bend parameter p with the same effective radius R_{eff} and $\alpha < 180^\circ$, such that the general findings of the optimization hold also true for elevated propagation losses. For loss mechanisms such as strong absorption and scattering, which might be critical for other photonic integrated platforms, supplementary terms can be included in the employed numerical analysis approach. The cross section of the embedded waveguide is set to $700 \text{ nm} \times 160 \text{ nm}$, which ensures single mode operation. The influence of the bend geometry on the loss is investigated for the more sensitive TM-like polarized guided mode. Bend loss for TE-like polarization are in general smaller compared to the TM-like polarization because the confinement of the TE-like mode is higher and radiative losses are reduced. Therefore, in PIC designs where both polarizations are present in the optical path the TM-like polarization typically dictates the minimum usable effective bend radius. Figures 1(b)-1(d) depict the investigated 45° , 90° , and 180° partial Euler bend geometries for the bend parameter value $p = 0.2$.

The EME method was benchmarked against finite-difference-time-domain (FDTD) calculations (Lumerical) for 90° bends with an effective radius of $40 \mu\text{m}$. Figure 3 compares the bend losses calculated by both FDTD and EME for different bend parameter p . The results agree within 0.01 dB, or 7%, respectively. This confirms that the employed EME method is a suitable alternative to FDTD allowing computationally efficient calculations of waveguide bend losses.

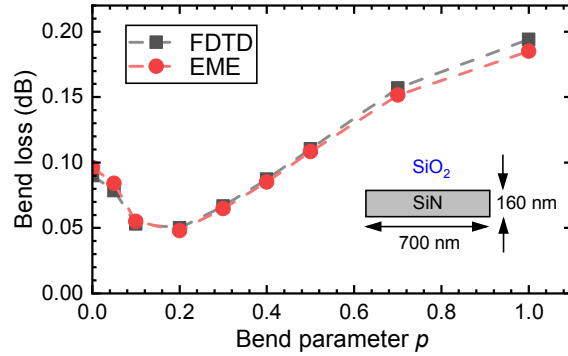


Fig. 3. Total bend loss determined by eigenmode expansion (EME) and finite-difference-time-domain (FDTD) method for 90° bends, $40 \mu\text{m}$ effective radius, and TM-like polarization.

3.2. Results and discussion of numerical analysis

Figure 4 summarizes the calculated total bend loss for the guided mode propagation through a 45° partial Euler bend with varying bend parameter p . A bend parameter of $p = 0.3$ provides optimal performance for the studied radii. For instance, the bend loss for $R_{\text{eff}} = 40 \mu\text{m}$ can be reduced to 0.07 dB ($p = 0.3$) compared to 0.09 dB ($p = 0$) and 0.14 dB ($p = 1$). The loss through an S-bend geometry, consisting of a second rotated congruent bend, can be readily obtained by squaring the transfer function or doubling the loss of a single bend, respectively.

Figure 5(a) summarizes the numerical results of the calculated bend losses through 90° bends. The results show a minor influence of the bend parameter $p > 0.2$ for effective bend radii R_{eff} larger than approximately $70 \mu\text{m}$. However, for $p < 0.2$ the transition from the straight to the bent waveguide section is no longer adiabatic and the total bend loss increases from 0.001 dB ($p = 0.2$) for an optimized bend to 0.026 dB ($p = 0$) for a purely circular bend. At $R_{\text{eff}} = 40 \mu\text{m}$ the total bend loss is 0.05 dB for $p = 0.2$, compared to 0.10 dB for a circular bend ($p = 0$), and 0.19 dB for a pure Euler bend ($p = 1$). One can notice that the loss through two 45° bends in a

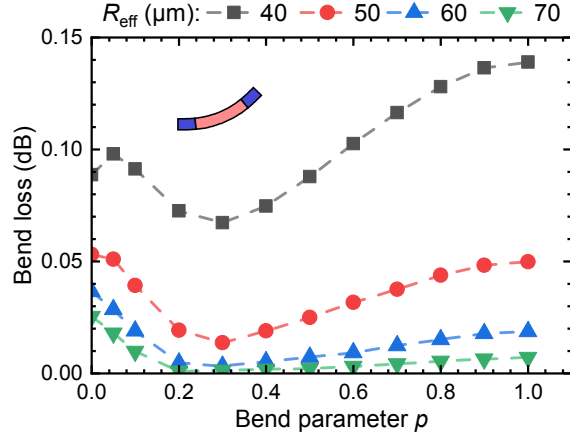


Fig. 4. Total bend loss through a 45° partial Euler bend for different bend radii, TM-like polarization. Inset depicts the bend geometry.

S-bend structure will be larger than through a single 90° bend for the same effective bend radius as the number of transitions from straight to bend waveguide sections is doubled in an S-bend structure.

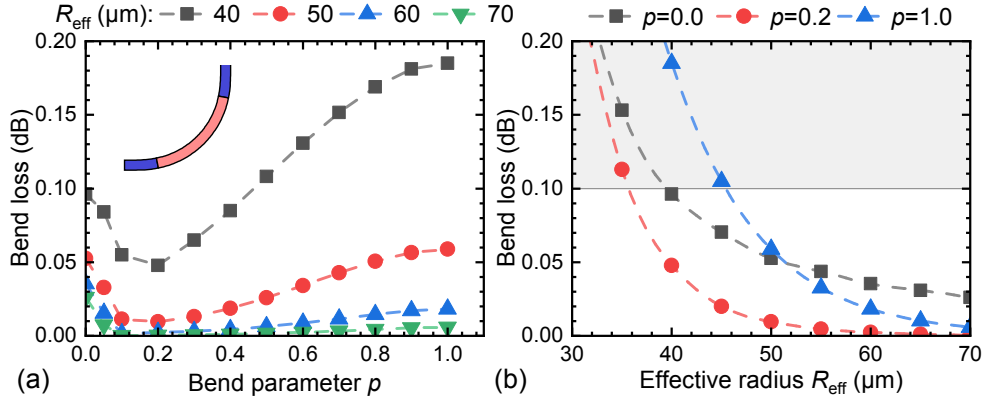


Fig. 5. Total bend loss through a 90° partial Euler bend, TM-like polarization. (a) Variation of bend parameter p for different effective bend radii. (b) Variation of effective bend radius R_{eff} for different values of the bend parameter p . The area with loss larger than 0.1 dB is indicated in grey for visualization.

Figure 5(b) summarizes the total bend loss of a circular bend, an optimized Euler bend ($p = 0.2$), and a pure Euler bend ($p = 1$) for a varying effective radius R_{eff} . The optimized Euler bend provides the smallest losses over the studied range of effective bend radii. One can observe that for bend radii larger than $50 \mu\text{m}$ a pure Euler bend is beneficial compared to a circular bend. However, below this radius, the reduced transition losses compared to the circular bend no longer compensate for the increasing radiative bend mode losses from the larger curvature of the pure Euler bend, resulting in a better performance of the circular bend compared to a pure Euler bend. For a targeted loss value of 0.1 dB per bend, the effective bend radii are found to be $36 \mu\text{m}$ ($p = 0.2$), $39 \mu\text{m}$ ($p = 0$), and $45 \mu\text{m}$ ($p = 1$), respectively. Therefore, an optimized partial Euler bend can increase the component integration density for the given example by a factor of 1.17

relative to a circular bend. For comparison, if we choose the targeted loss value based on the loss of a $70\ \mu\text{m}$ circular bend of $0.026\ \text{dB}$ per bend, the partial Euler bend with the same loss has an effective radius of $43\ \mu\text{m}$ ($p = 0.2$) and $57\ \mu\text{m}$ ($p = 1$), respectively, leading to an improvement in integration density by a factor of 2.7 compared to a circular bend, and a factor of 1.8 compared to a pure Euler bend.

Figure 6(a) to Fig. 6(d) depict the individual contributions of the two loss mechanisms, i.e., transition and radiative bend mode losses, to the total bend loss along the bend for an effective radius of $R_{\text{eff}} = 40\ \mu\text{m}$ and four distinct values of the bend parameter ($p = 1$, $p = 0.2$, $p = 0.05$, $p = 0$). The optimized partial Euler bend ($p = 0.2$) balances radiative bend mode losses arising from sections of high curvature with transition losses from sections of rapidly changing curvature.

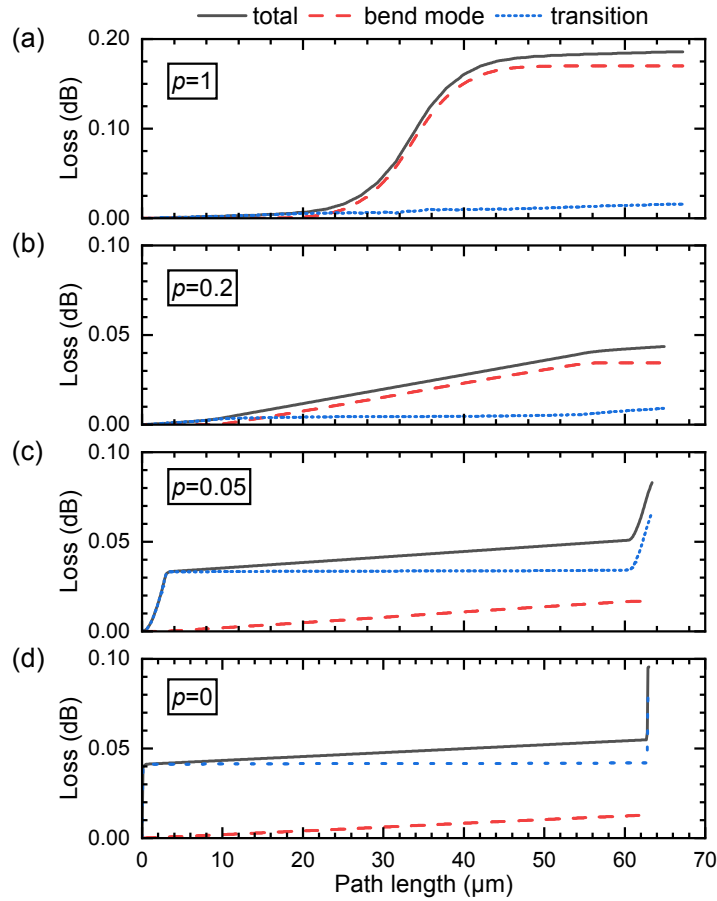


Fig. 6. Bend mode radiative, transition, and total losses accumulated along 90° partial Euler bends with effective radius of $40\ \mu\text{m}$ for (a) $p = 1$, (b) $p = 0.2$, (c) $p = 0.05$, and (d) $p = 0$. The scale in (a) for the loss has twice the range than (b)-(d) for better visualization. An optimized partial Euler bend ($p = 0.2$) distributes the accumulated loss along the bend. In contrast, a pure Euler bend ($p = 1$) suffers from high radiative losses in the middle of the bend where curvatures are large. The geometry with $p = 0.05$ is close to a circular bend ($p = 0$) and the transition losses in the Euler sections are the major loss.

Transition losses are not limited to the case of a discontinuous jump in curvature, which occurs for example at the interface between the straight input and bend section of a circular bend, but are present whenever a change in curvature $d\kappa/ds$ is present. In the circular middle section of

a partial Euler bend, no transition losses occur ($d\kappa/ds = 0$) and only the radiative bend mode components contribute to the loss. In contrast to the optimized bend, the pure Euler bend ($p = 1$) exhibits large radiative bend mode losses at the middle of the bend originating from the increased curvature compared to a circular or partial Euler bend leading to significant total losses. The bend geometry with $p = 0.05$ is close to a circular bend and has high losses at the start and end of the bend, where the transition loss arising from the fast changing curvature contribute most to the total loss. On the other hand, radiative bend mode losses are small for this geometry, as the minimal radius of curvature is larger than the minimal radius of curvature of the optimized and pure Euler bend.

Like the 90° bend, the 180° bend shows lowest loss for a partial Euler bend with the parameter p around 0.2. The bend loss decreases from 0.083 dB to 0.047 dB for an effective bend radius of $R_{\text{eff}} = 40 \mu\text{m}$. Figure 7 shows the bend loss for effective bend radii ranging from $40 \mu\text{m}$ to $70 \mu\text{m}$. In contrast to 45° and 90° bends, the minimum radius of curvature R_{min} of a 180° bend is close to a circular bend for all p . This results in a reduced dependence of the bend loss on the partial Euler bend parameter for $p > 0.2$.

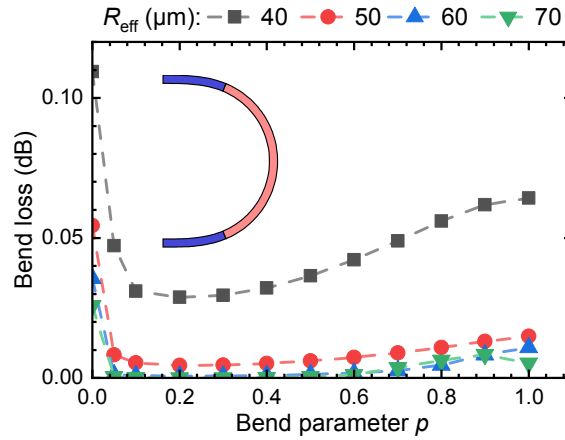


Fig. 7. Total bend loss through 180° Euler bends, TM-like polarization. Inset depicts the bend geometry.

In summary, the findings underline that the implementation of a pure Euler bend and other classes of bend geometries with sections of small radius of curvature can introduce pronounced radiative bend mode losses. Compared to a pure Euler bend a partial Euler bend increases the minimum radius of curvature R_{min} at the expense of transition losses. This trade-off reduces the total bend loss. It has to be pointed out that the optimized values for the Euler bend parameter p are specific to the investigated waveguide system. The waveguide geometry, the material refractive indices, the wavelength, and the polarization determine the confinement of the guided mode and, thus, strongly influence the radiation properties of curved waveguides. Therefore, a dedicated optimization for a specific waveguide system, effective bend radius, and polarization is mandatory. For a 90° partial Euler bend on silicon photonic platform Fujisawa et al. obtained an optimal ratio of 68 % between the Euler section length and the total bend length with a radius of $R_{\text{eff}} = 3 \mu\text{m}$ for the TE-like polarized mode at a wavelength of $1550 \mu\text{m}$ [26]. This value corresponds to $p = 0.52$ in our parameterization, which is considerably larger than the value of $p = 0.2$ at $R_{\text{eff}} = 40 \mu\text{m}$ in our study for a silicon nitride photonic platform.

4. Experimental analysis

4.1. Fabrication and optical characterization

Partial Euler bends of 90° with an effective radius of $50\ \mu\text{m}$ and different values of the bend parameter p have been fabricated on a SiN photonic platform [39]. The SiN waveguide layer has a nominal thickness of 160 nm. Figure 8(a) shows a microscope image of these structures. The width of the waveguide was measured by scanning electron microscopy to be 680 nm. The waveguide cross-section ensures single mode operation. Refractive indices of the SiO_2 cladding and the SiN waveguide material have been determined by ellipsometry to be $n_{\text{SiO}_2} = 1.46$ and $n_{\text{SiN}} = 1.92$ at a wavelength of 850 nm. The test structures consist of 240 cascaded 90° bends for the TE-like polarization. Each bend is separated from the subsequent bend by a $10\ \mu\text{m}$ straight segment. To account for the high bend losses for the TM-like polarization, a cleaved sample with four bends for the TM-like polarization was prepared.

To characterize the bend losses light from a 850 nm Ti:sapphire laser source was end-face coupled via a polarization maintaining fiber (NA 0.12) to the waveguides with the bend structures. The polarization plane of the fiber was adjusted with a mechanical rotator and verified using a linear polarizer in combination with an optical power meter to couple to the TE-like and TM-like PIC waveguide mode, respectively. The output light of the PIC was collected with a single mode fiber (NA 0.12) connected to an optical power meter. The positioning of the input and output fibers to the PIC was supported by a piezoelectric auto alignment system (Thorlabs, NanoTrak®). The repeatability of the transmission power level measurement was better than 0.2 dB. A reference waveguide without bends was used to account for the efficiency of the end-face fiber coupling into and out of the PIC, and the propagation loss from the routing of the optical signals. The difference of transmitted optical power between the waveguide with the bend structures and the reference waveguide is divided by the number of bends, i.e. 240 for the TE-like and 4 for the TM-like mode, to calculate the loss of a single bend. The numerical simulations include propagation losses of 0.7 dB for the TE-like and 0.4 dB for the TM-like mode [8].

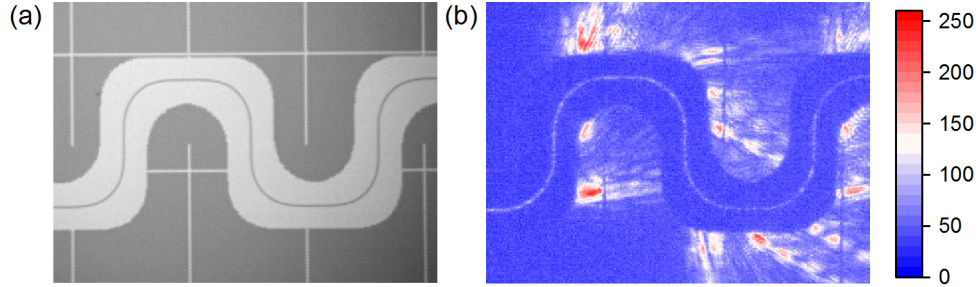


Fig. 8. (a) Microscope image of fabricated SiN partial Euler bends with an effective radius $50\ \mu\text{m}$. (b) Near-infrared image of radiation emitted from the bends and scattered at the lithography fill pattern.

4.2. Results and discussion of experimental analysis

The radiation arising from the transition losses and bend waveguide modes for the TM-like polarization was recorded with an infrared camera (Hamamatsu, IR Vidicon C2741) and is visualized in Fig. 8(b). The light enters the bend structure from the left handside. Strong radiation patterns are visible at each bend. Tracing the streaks back to the source suggests the main contribution from the middle of the bend, where the curvature is largest.

Figures 9(a) and 9(b) summarize the influence of the bend parameter p on the total bend losses in TE-like and TM-like polarization, respectively. For the TE-like polarization the mode mismatch between the straight and bend section is a major loss component and the largest bend losses occur, hence, for a circular bend with 0.028 dB per bend. With an optimized partial Euler bend, the bend loss is reduced to 0.007 dB at $p = 0.2$. For larger values of the bend parameter p , the losses start to slowly increase. The numerical simulations with the EME method reflect the measurements to a high degree. For the TM-like waveguide mode the major losses arise from the radiative bend modes. Therefore, the optimal bend geometry converges to a circular bend at which the radius of curvature is maximized. A pure Euler bend ($p = 1$) is detrimental to the bend performance. The offset between experiment and numerical analysis for the TM-like polarization can most likely be attributed to the effective thin film thickness of the SiN waveguide layer, as the bend losses of the TM-like mode are highly sensitive to variations of the waveguide geometry. For example, a small change of the waveguide height in the simulations from 160 nm to 158 nm increases the bend loss of the TM-like mode by 0.2 dB for a pure Euler bend. This results in an improved agreement with the measured values. For the TE-like mode, the simulation results indicate a much lower influence of the waveguide height on the bend losses. Overall, the TM-like mode shows increased bend losses of up to two magnitudes higher than the TE-like polarization for the chosen bend radius, which underlines the importance to optimize the TM-like mode in mixed polarization designs.

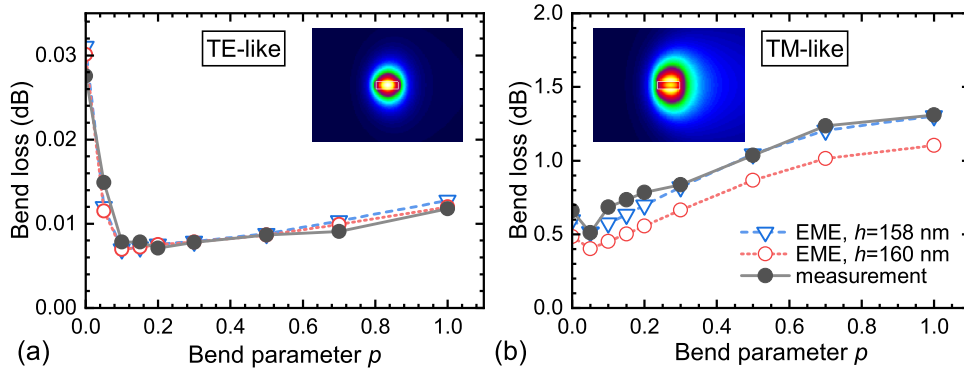


Fig. 9. Total bend loss measurement and numerical results through 90° partial Euler bends with effective radius of $50 \mu\text{m}$ for (a) TE-like and (b) TM-like waveguide mode. Insets show the bend waveguide profile for the major electric field components at the smallest radius of curvature of an Euler bend.

The SiN of the employed PIC technology platform has a refractive index which is 5% smaller than the value taken from literature and used in the numerical analysis in the previous section. This moderate difference in refractive index causes a strong increase of the minimum bend loss for the $50 \mu\text{m}$ bends in the TM-like polarization from 0.01 dB to 0.5 dB due to the reduced confinement strength of the waveguide mode. Furthermore, the optimum value of the bend parameter found for the fabricated bends shifts towards zero, i.e. a circular bend, because the bend mode losses play a more important role than for the mode in the theoretical analysis with the higher SiN refractive index. This is in accordance with the prediction made by the EME calculations.

5. Conclusion

In this work the major loss mechanisms for partial Euler bend geometries were numerically analyzed with the EME method. This method provides additional insights, not accessible with

other tools, into the individual contributions to the total loss along the geometry. Optimal values for the bend parameter have been identified for 45°, 90° and 180° silicon nitride waveguide partial Euler bends operated with TM-polarization using literature values for the refractive indices at an operation wavelength of 850 nm. The proper choice of the bend parameter balances transition losses arising from the continuous transition between sections of changing curvature, and radiative losses originating from the curvature of the bend waveguide mode. Transition losses are not limited to the abrupt change between a straight and a bent section, but occur whenever the curvature is changing non-adiabatically, e.g. for all bends with a significantly fast change in curvature. Compared to a pure Euler bend without a section of constant curvature, an optimized partial Euler bend exhibits a reduced bend loss. With a partial Euler waveguide bend geometry the integration density of PICs can be increased and losses for complex designs relying on a large number of bends reduced. The numerical analysis has been applied to fabricated partial Euler bends for a specific silicon nitride photonic platform. The measurements of the bend losses agree well with the EME simulations and confirm the feasibility of this method to optimize waveguide bends for a specific material system and waveguide geometry. The small differences between the refractive indices assumed in the theoretical study and the experimental photonic platform showed a considerable impact on the optimal value of the bend parameter and on the actual loss values. Our findings emphasize that the optimal ratio between the Euler section to the total bend length has to be determined individually for different waveguide systems.

Funding

Austrian Research Promotion Agency (FFG) (850649); European Union's Horizon 2020 research and innovation programme (688173).

Acknowledgments

This research has received funding through the grant PASSION (No. 850649) from the Austrian Research Promotion Agency (FFG) and European Union's Horizon 2020 research and innovation programme under the grant OCTCHIP (No. 688173).

Disclosures

The authors declare no conflicts of interest.

References

1. Y. Vlasov, "Silicon CMOS-integrated nano-photonics for computer and data communications beyond 100G," *IEEE Commun. Mag.* **50**, S67–S72 (2012).
2. Q. Cheng, M. Bahadori, M. Glick, S. Rumley, and K. Bergman, "Recent advances in optical technologies for data centers: a review," *Optica* **5**, 1354 (2018).
3. J. Bland-Hawthorn and P. Kern, "Astrophotonics: a new era for astronomical instruments," *Opt. Express* **17**, 1880–1884 (2009).
4. B. Norris and J. Bland-Hawthorn, "Astrophotonics: The rise of integrated photonics in astronomy," *Opt. Photonics News* **30**, 26 (2019).
5. C. Ciminelli, F. Dell'Olio, D. Conteduca, and M. N. Armenise, "Silicon photonic biosensors," *IET Optoelectronics* **13**, 48–54 (2019).
6. H. Jans, P. O'Brien, I. Artundo, R. Hoofman, D. Geuzebroek, P. Dumon, M. van der Vliet, J. Witzens, E. Bourguignon, P. van Dorpe, L. Lagae, and M. A. G. Porcel, "Integrated bio-photonics to revolutionize health care enabled through pix4life and pixapp," *Proc. SPIE* 10506, 105060V (2018).
7. S. Talebi Fard, S. M. Grist, V. Donzella, S. A. Schmidt, J. Flueckiger, X. Wang, W. Shi, A. Millsbaugh, M. Webb, D. M. Ratner, K. C. Cheung, and L. Chrostowski, "Label-free silicon photonic biosensors for use in clinical diagnostics," *Proc. SPIE* 8629, 862909 (2013).
8. R. Hainberger, P. Muellner, S. Nevlacsil, A. Maese-Novo, F. Vogelbacher, M. Eggeling, J. Schotter, M. Sagmeister, G. Koppitsch, and J. Kraft, "Silicon-nitride waveguide-based integrated photonic circuits for medical diagnostic and other sensing applications," *Proc. SPIE* 10922, 1092204 (2019).

9. F. Lenzini, N. Gruhler, N. Walter, and W. H. P. Pernice, "Diamond as a platform for integrated quantum photonics," *Adv. Quantum Technol.* **1**, 1800061 (2018).
10. T. Kitoh, N. Takato, M. Yasu, and M. Kawachi, "Bending loss reduction in silica-based waveguides by using lateral offsets," *J. Light. Technol.* **13**, 555–562 (1995).
11. A. Melloni, P. Monguzzi, R. Costa, and M. Martinelli, "Design of curved waveguides: The matched bend," *J. Opt. Soc. Am. A* **20**, 130 (2003).
12. M. Harjanne and T. Aalto, "Design of tight bends in silicon-on-insulator ridge waveguides," *Phys. Scripta* **T114**, 209–212 (2004).
13. J. H. Song, T. D. Kongnyuy, A. Stassen, V. Mukund, and X. Rottenberg, "Adiabatically bent waveguides on silicon nitride photonics for compact and dense footprints," *IEEE Photonics Technol. Lett.* **28**, 2164–2167 (2016).
14. H. Wu, C. Li, L. Song, H.-K. Tsang, J. E. Bowers, and D. Dai, "Ultra-sharp multimode waveguide bends with subwavelength gratings," *Laser & Photonics Rev.* **13**, 1800119 (2019).
15. P.-L. Liu, B.-J. Li, P. J. Cressman, J. R. Debesis, and S. Stoller, "Comparison of measured losses of Ti:LiNbO₃ channel waveguide bends," *IEEE Photonics Technol. Lett.* **3**, 755–756 (1991).
16. A. Iguchi, Y. Tsuji, T. Yasui, and K. Hirayama, "Topology optimal design for optical waveguides using time domain beam propagation method," *IEICE Electron. Express* **15**, 20180417 (2018).
17. L. H. Gabrielli, D. Liu, S. G. Johnson, and M. Lipson, "On-chip transformation optics for multimode waveguide bends," *Nat. Commun.* **3**, 1217 (2012).
18. C. Koos, C. G. Poulton, L. Zimmermann, L. Jacome, J. Leuthold, and W. Freude, "Ideal bend contour trajectories for single-mode operation of low-loss overmoded waveguides," *IEEE Photonics Technol. Lett.* **19**, 819–821 (2007).
19. Y. Liu, K. Xu, S. Wang, W. Shen, H. Xie, Y. Wang, S. Xiao, Y. Yao, J. Du, Z. He, and Q. Song, "Arbitrarily routed mode-division multiplexed photonic circuits for dense integration," *Nat. Commun.* **10**, 3263 (2019).
20. T. Chen, H. Lee, J. Li, and K. J. Vahala, "A general design algorithm for low optical loss adiabatic connections in waveguides," *Opt. Express* **20**, 22819–22829 (2012).
21. M. Bahadori, M. Nikdast, Q. Cheng, and K. Bergman, "Universal design of waveguide bends in silicon-on-insulator photonics platform," *J. Light. Technol.* **37**, 3044–3054 (2019).
22. American Railway Engineering and Maintenance-of-Way Association, *Practical Guide to Railway Engineering* (AREMA, 2003).
23. W. Kühn, *Fundamentals of road design* (WIT, 2013).
24. M. Cherchi, S. Ylinen, M. Harjanne, M. Kapulainen, and T. Aalto, "Dramatic size reduction of waveguide bends on a micron-scale silicon photonic platform," *Opt. Express* **21**, 17814–17823 (2013).
25. X. Jiang, H. Wu, and D. Dai, "Low-loss and low-crosstalk multimode waveguide bend on silicon," *Opt. Express* **26**, 17680 (2018).
26. T. Fujisawa, S. Makino, T. Sato, and K. Saitoh, "Low-loss, compact, and fabrication-tolerant Si-wire 90° waveguide bend using clothoid and normal curves for large scale photonic integrated circuits," *Opt. Express* **25**, 9150–9159 (2017).
27. M. H. P. Pfeiffer, J. Liu, A. S. Raja, T. Morais, B. Ghadiani, and T. J. Kippenberg, "Ultra-smooth silicon nitride waveguides based on the damascene reflow process: fabrication and loss origins," *Optica* **5**, 884 (2018).
28. M. A. Porcel, A. Hinojosa, H. Jans, A. Stassen, J. Goyvaerts, D. Geuzebroek, M. Geiselmann, C. Dominguez, and I. Artundo, "Silicon nitride photonic integration for visible light applications," *Opt. & Laser Technol.* **112**, 299–306 (2019).
29. P. Muñoz, J. D. Domenech, C. Domínguez, A. Sánchez, G. Micó, L. A. Bru, D. Pastor, J. Fernández, and J. M. Cirera, "Silicon nitride photonics: from visible to mid-infrared wavelengths," *Proc. SPIE* 10537, 105370B (2018).
30. M. Ren, J. Pu, V. Krishnamurthy, L. Gonzaga, Y. T. Toh, F. Tjiptoharsono, Y. Yang, K. T. D. Ng, and Q. Wang, "A theoretical and experimental study of silicon Y-branch micro-loop reflectors," *IEEE Photonics Technol. Lett.* **28**, 2811–2814 (2016).
31. Y. Zhang, S. Yang, H. Guan, A. E.-J. Lim, G.-Q. Lo, P. Magill, T. Baehr-Jones, and M. Hochberg, "Sagnac loop mirror and micro-ring based laser cavity for silicon-on-insulator," *Opt. Express* **22**, 17872–17879 (2014).
32. F. W. J. Olver, *NIST handbook of mathematical functions* (Cambridge University, 2010).
33. R. Bulirsch, "Numerical calculation of the sine, cosine and Fresnel integrals," *Numer. Math.* **9**, 380–385 (1967).
34. W. H. Press, *Numerical recipes: The art of scientific computing* (Cambridge University, 2007).
35. M. Alazah, S. N. Chandler-Wilde, and S. La Porte, "Computing Fresnel integrals via modified trapezium rules," *Numer. Math.* **128**, 635–661 (2014).
36. D. F. G. Gallagher and T. P. Felici, "Eigenmode expansion methods for simulation of optical propagation in photonics: pros and cons," *Proc. SPIE* 4987, 69–89 (2003).
37. K. Luke, Y. Okawachi, M. R. E. Lamont, A. L. Gaeta, and M. Lipson, "Broadband mid-infrared frequency comb generation in a Si₃N₄ microresonator," *Opt. letters* **40**, 4823–4826 (2015).
38. L. V. Rodríguez-de Marcos, J. I. Larruquert, J. A. Méndez, and J. A. Aznárez, "Self-consistent optical constants of SiO₂ and Ta₂O₅ films," *Opt. Mater. Express* **6**, 3622 (2016).
39. M. Sagmeister, G. Koppitsch, P. Muellner, S. Nevlacsil, A. Maese-Novo, R. Hainberger, D. Seyringer, and J. Kraft, "Monolithically integrated, CMOS-compatible SiN photonics for sensing applications," *Proceedings* **2**, 1023 (2018).